Applied Physics A (2023) 129:158
https://doi.org/10.1007/s00339-023-06449-9

Applied Physics A
Materials Science & Processing

Supercapacitor performance of vanadium-doped nickel hydroxide microflowers synthesized using the chemical route

D. B. Mane[1,2,3] · O. C. Pore[1] · D. S. Sawant[1] · D. V. Rupnavar[1] · R. V. Shejwal[1] · S. H. Mujawar[4] · L. D. Kadam[2] · R. V. Dhekale[3] · G. M. Lohar[1]

Received: 15 August 2022 / Accepted: 24 January 2023 / Published online: 1 February 2023

Abstract

A supercapacitor is a high-capacity device that interfaces electrolytic capacitors and batteries by possessing a capacitance value significantly larger than conventional capacitors but with lower voltage limits. Nickel hydroxide is a potential material exhibiting tempting properties such as high specific capacitance, various oxidation states, morphologies, and large surface area. However, various limitations must be overcome, such as increasing the current density and improving the stability after doping of vanadium in $Ni(OH)_2$ material-doped $Ni(OH)_2$microflowers were successfully fabricated using a chemical bath deposition process in this study. XRD studies show hexagonal crystal structure with γ-phase of $Ni(OH)_2$. The presence of V=O at peak positions 1023, and 923 cm^{-1} reveals in the FT-IR study. Increased interlayer distance demonstrates the presence of vanadium ions between the superior and inferior layers of $Ni(OH)_2$. The 0.3% V-doped $Ni(OH)_2$ electrode displayed a remarkable specific capacitance of 1456.8 F g^{-1} at 3 mA cm^{-2} and high performance with 88.17% capacity retention at a scan rate of 100 mV s^{-1} over 2000 cycles.

Keywords Nickel hydroxide · Vanadium doping · Microflower · Supercapacitor

1 Introduction

Nickel-based materials are utilized in batteries and supercapacitors [1]. The nickel-based material is in high demand for supercapacitor designs. Nickel oxides [2], hydroxides [3–5], sulphides [6, 7], and selenium [8] are used to make supercapacitors. Excellent electrochemical properties and environmental friendliness have made nickel hydroxide a strong contender in the list of supercapacitors [9, 10]. The specific capacitance of nickel hydroxide does not rise above a certain value and is not stable in alkaline solutions [11]. A better option to overcome the above problem is to develop nanomaterials [12, 13] or doping the transition metal with higher electrical conductivity and stability [14]. Different dimensional nanostructures were developed by chemical methods like sol–gel [15, 16], solvothermal [17], electrodeposition [18], microemulsion [19], templet-derived method [16], etc. nanoparticles are used for different practical applications such as supercapacitor, photocatalyst [20], and antibacterial properties [21]. Cobalt [22], yttrium [23], aluminium [24], phosphorus [25], manganese [26], iron [27], etc., these metals are doped in nickel hydroxide, and their compositional, morphological, and electrochemical properties change to a great extent. Doping a metal will increase its electrical conductivity and stability properties.

Zhang et al. [26] used a doping approach to increase the specific capacitance of nickel hydroxide. Researchers realize that manganese is a better option for increasing specific capacity. The hydrothermal approach was used to make Mn-doped $Ni(OH)_2$ using $Ni(NO_3)_2$ as a nickel source and $Mn(CHCOO)_2$ as a manganese precursor. Hexamethylenetetramine surfactant was utilized to control the rate of reaction, and a deposition temperature of 100 °C was maintained for 2 h. Nanosheets with a height of 200–300 nm are cross-connected during this reaction,

✉ G. M. Lohar
gauravlohar24@gmail.com

[1] Department of Physics, Lal Bahadur Shastri College of Arts, Science and Commerce, Satara, MS 415002, India

[2] Department of Physics, Arts, Commerce and Science College, Ramanadnagar (Burli), Sangli, MS 416308, India

[3] Department of Physics, Kisan Veer Mahavidyalaya, Wai, MS 412803, India

[4] Department of Physics, Yashwantrao Chavan Institute of Science, Satara, MS, India

but there is no complex nanostructure present to give a substantial surface area for electrolyte interaction. Hussain et al. [27] have successfully deposited Fe-doped ultrathin curled nanosheets that will be used for water splitting in future fuel and supercapacitor applications. As the prepared nanosheets of Fe-doped $Ni(OH)_2$ have a high 'd' value hence, the effective surface area increases, leading to the mesoporous nature of the material. The mesoporous material has three times the energy density of ruthenium oxide. Doping had the added benefit of widening the potential window. Current and power density of the undoped electrode is 67.4 Wh kg^{-1} and 16 W kg^{-1}, respectively and after Fe doping, the values, are 400 Wh kg^{-1} and 40 W kg^{-1}. Fe-doped nickel hydroxide has a specific capacitance value of 1503 F g^{-1} and stability is increased by 86% after 9000 cycles. Zhu et al. [23] tried to solve some of the drawbacks of $Ni(OH)_2$ such as low electrical conductivity and stability. The researchers claim that if a metal with high conductivity is added to a lattice with low conductivity, the conductivity of the material increases. Due to doping, such a suitable metal can be added to the nickel hydroxide material. Accordingly, doping can promote the ion diffusion rate and electron transport conductance. Vanadium has many oxidation states that affect electrochemical properties [28, 29]. With different oxidation states like + 3, + 4, and + 5 different compounds are formed like VO_2, V_2O_3, and V_2O_5 show different electrochemical behavior [30, 31]. Vanadium oxide has a wide potential window up to 0.0–0.8 V vs SCE [30]. The theoretical value of specific capacitance lies between 1000 and 2000 F g^{-1} [29]. Many nanostructures were formed with vanadium oxide like hollow spheres [32], nanoflakes or nanowalls [33–35], nanotubes, or nanorods [36, 37], nanobelt [38], microflower [39], etc.

By observing the literature, there is scope to develop the vanadium-doped nickel hydroxide and study its supercapacitor performance. After studying extensive literature there is not any relevant reference found on vanadium-doped in nickel hydroxide and study their supercapacitor performance. The chemical bath deposition (CBD) method uses to deposit vanadium-doped nickel hydroxide material. Then structural and morphological investigations are carried out by utilizing XRD, FTIR, and SEM. To study the supercapacitor performance EIS, CV, and charge–discharge have been employed. The 0.3% V-doped $Ni(OH)_2$ electrode displayed a remarkable specific capacitance of 1456.8 F g^{-1} at 3 mA cm^{-2} and high rate performance with 88.17% capacity retention at scan rate 100 mV s^{-1} over 2000 cycles. The present study shows vanadium-doped $Ni(OH)_2$ exhibits battery type with a high rate of diffusion. As a result, vanadium-doped $Ni(OH)_2$ is a promising alternative for improved energy density and stability in battery-type supercapacitors.

2 Experimental details

2.1 Chemicals

Even without purification, AR-grade chemicals from Thomas Beaker Chemical Pvt. Ltd. in Mumbai were used in the synthesis of V-doped $Ni(OH)_2$. For the deposition of thin films, nickel sulphate hexahydrate ($NiSO_4.6H_2O$) and vanadyl sulphate ($VOSO_4.XH_2O$) were used as a source of Ni and V ions, respectively. Ammonium hydroxide (NH_4OH, 30%) was used as a hydroxide ion source. Potassium persulphate ($K_2S_2O_8$) was used as the oxidizing agent.

2.2 Bath preparation

As current collectors, vanadium-doped nickel hydroxide samples have been successfully synthesized using the CBD method on stainless-steel substrates. First, a solution of 1 M nickel sulfate in 40 ml and 1 M vanadyl sulfate in 10 ml in double distilled water was prepared. By volume concentration method, 0.2% nickel sulfate solution was removed and an equal volume of vanadyl sulfate solution was added. In such a manner a solution of 0.2% vanadium-doped nickel sulphate was prepared. A solution of 0.25 M $K_2S_2O_8$ in 30 mL DDW was prepared and poured into the above solution after stirring for some time. Pour 20 mL of DDW solution into it and after a while add 10 mL of ammonia then stir again for a few minutes. Similarly prepare a bath solution of concentration 0.3, 0.4% vanadium-doped $Ni(OH)_2$ solution. Now finally, dip the precleaned stainless steel substrate in that solution with the help of the holder. Remove the stainless steel substrate from the solution after 120 min and rinse it several times then let it dry naturally. Heat the fully dried films to 100 °C for 2 h.

2.3 Growth mechanism

An apple-green solution of $NiSO_4$ and $VOSO_4$ turns dark blue-black when mixed with aqueous ammonia. When the steel substrates are immersed in the solution, the material is deposited on the substrate in three steps. In the first step, different ions react with each other and a monolayer of metal chalcogenide is deposited on the surface of the substrate [12]. In the second step, the monolayer acts as a catalytic surface then the metal ions are attracted. Condensation begins and the film grows on the substrate. Film growth depends on bath parameters. After a certain time, the terminal phase growth of the film stops [13]. Ni^{2+} ions react with ammonia to form $Ni(OH)_2$ shown in the chemical reaction through Eqs. 1, and 2, respectively.

$$\left[Ni\left(H_2O\right)_{6-x}\left(NH_3\right)_x\right]^{2+} \rightarrow Ni(OH)_2 + (6-x)H_2O + xNH_3 \quad (1)$$

$$2\,Ni(OH)_2 + S_2O_8^{2-} \rightarrow 2\,NiOOH + 2SO_4^{2-} + 2H^+. \quad (2)$$

Potassium persulfate plays an important role in oxidizing agents by removing a hydrogen atom from $Ni(OH)_2$ to form NiOOH. Simultaneously, persulfate ions play the role of the directing agent which controlled the morphological structure growth. This lowers the surface energy along a specific growth axis [14]. Hence the growth of a specific axis of the morphological structure is stunted. Since the doping concentration is very low and the vanadium ion is large, it is placed in two layers of $Ni(OH)_2$ material rather than entering the crystal structure of nickel hydroxide. For doping 0%, 0.2%, 0.3%, and 0.4% vanadium doping the obtained films were named V-0, V-1, V-2, and V-3, respectively.

3 Results and discussion

3.1 X-ray diffraction study

Figure 1 includes the XRD patterns of samples V-0, V-1, V-2, and V-3. The XRD peak data closely matches the standard JCPDS data (Card No. 22-0444) [40]. The structure of $Ni(OH)_2$ is illustrated in Fig. 2a, b with space group P-31 m and crystal lattice parameters taken from a JCPDS card. In XRD patterns, different peaks show angles of 12, 33.4, 43, 44, 59.77, 74.6, and 90°. The peaks corresponding to $Ni(OH)_2$ appear at angles of 12, 33.4, and 59.77° correspond to the planes of (0 0 1), (1 1 0), and (3 0 0), respectively. $Ni(OH)_2$ shows two polymorphs α and β. The β-polymorph has a close-packed hexagonal crystal structure but the α polymorph has more water molecules in the stacking plane of $Ni(OH)_2$. No significant peaks corresponding to vanadium species were detected in the XRD pattern. The atomic radius of vanadium (1.34×10^{-10} m) is greater than that of nickel (1.24×10^{-10} m), so during the reaction, the vanadium atom intercalates between two layers of nickel hydroxide without replacing the nickel in the crystal [23]. As the vanadium concentration increases, many vanadium ions intercalate between two layers of nickel hydroxides, increasing the interlayer spacing shown in Fig. 2c. Therefore, the intensity of nickel hydroxide peaks at 12, 33.4, and 59.77° decreases in the XRD pattern. The value of '*d*' for $Ni(OH)_2$ is 6.5 Å and for 0.2%, 0.3%, and 0.4% doping samples are 7.22, 7.29, and 7.32 Å, respectively. XRD analysis shows that the crystallinity of $Ni(OH)_2$ decreases with increasing doping concentration [23].

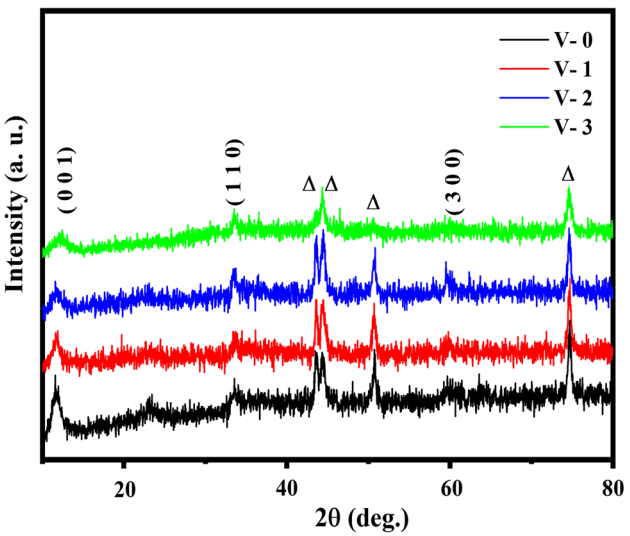

Fig. 1 X-ray diffraction pattern of electrodes V-0, V-1, V-2, and V-3

3.2 Fourier transform Infra-red spectroscopy (FT-IR)

Figure 3 shows the FT-IR analysis of electrodes V-0, V-1, V-2, and V-3. The seven sharp peaks were observed at 3536, 1610, 1138, 1023, 923, 606, and 435 cm^{-1}. The O–H stretching mode is indicated by the intense peak at wavenumber 3536 cm^{-1}. This indicates the presence of the free O–H group shows a brucite-like structure after heat treatment [41]. Bending vibration due to absorption of water molecule observed at peak 1610 cm^{-1}. Significant peaks observe at 435 cm^{-1} show Ni–O stretching of the bond [42]. The characteristics peak observed at 606 cm^{-1} shows confirmation of the bending vibration of Ni-OH [43]. Peaks at 1023, and 923 cm^{-1} show stretching vibration of the V=O bond [44, 45]. This peak confirmed the doping of vanadium in $Ni(OH)_2$ material.

3.3 Scanning electron microscopy

Figure 4a illustrates the growth of nanoflakes anchored vanadium-doped $Ni(OH)_2$ microflower. During the procedure, after the addition of ammonia solution becomes a precipitate then ions are attracted to the electron collector and deposited on the substrate. Nanoparticles clump together to form uniform-thickness nanoflakes. The microflower is formed when a large number of nanoflakes or nanosheets cluster together at the nucleation site. When vanadium is doped in solution vanadium ions are placed in between an adjacent layer of $Ni(OH)_2$ which makes the material less crystalline [40, 46]. So the thickness of nanoflakes increases. Potassium persulphate is used for dual purposes as an oxidant and structural guiding agent. During the reaction, $S_2O_8^{-2}$ ions generate a large number of adsorption sites, making it much easier for Ni^{2+} and OH^-ions to adhere to them. $K_2S_2O_8$ limits crystal crystallization along the Z-axis, resulting in a two-dimensional nanosheet structure. These nanosheets or nanoflakes become linked over time at nucleated sites, establishing

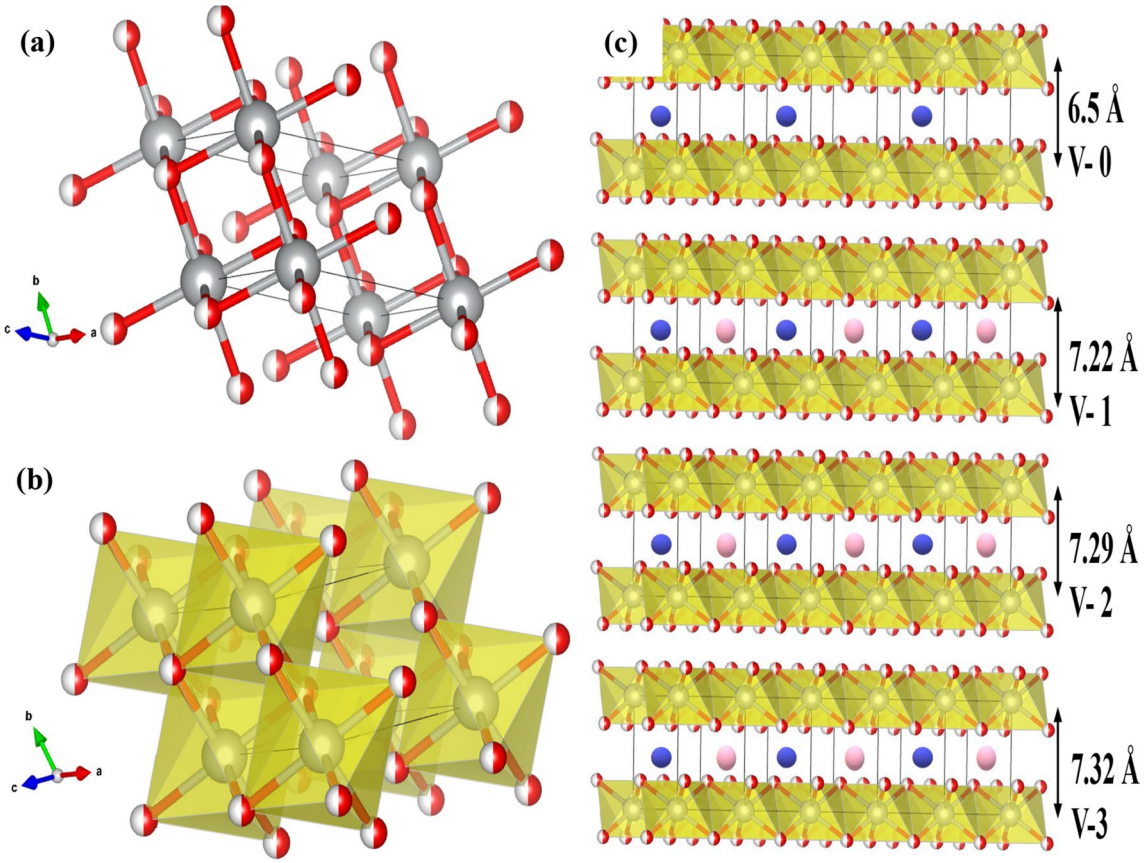

Fig. 2 Structural characterizations of vanadium-doped nickel hydroxide thin films for different doping concentrations (0.0%, 0.2%, 0.3%, and 0.4%). **a**, **b** Crystal structure of $Ni(OH)_2$. **c** Schematic demonstration of the value of interlayer distance varies concerning the concentration of vanadium doping

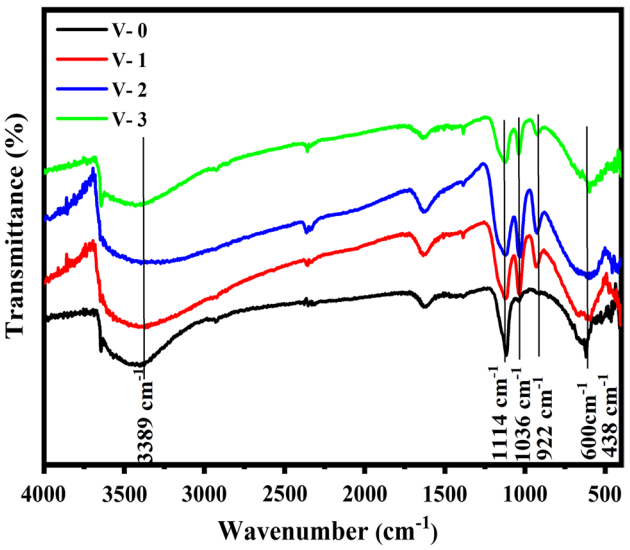

Fig. 3 FT-IR study of electrodes V-0, V-1, V-2, and V-3

a three-dimensional flower [47]. Figure 4b–e shows SEM images of microflowers of undoped, 0.2%, 0.3%, and 0.4% vanadium-doped $Ni(OH)_2$ samples. Figure 4.5b displays well-developed undoped $Ni(OH)_2$ microflowers with interconnected nanoflakes with a flake's thickness of 62.17 nm and a diameter of 4.27 µm. Figure 4.5c shows well-developed 0.2% vanadium-doped $Ni(OH)_2$ microflower with interconnected nanoflakes with flakes thickness of 66.19 nm and diameter of 6.61 µm. Figure 4.5d depicts a well-developed 0.3% vanadium-doped $Ni(OH)_2$microflower with linked nanoflakes ranging from 52.88 nm in thickness and 7.90 µm in diameter. Figure 4.5e shows a well-developed 0.4% vanadium-doped $Ni(OH)_2$ microflower with interconnected nanoflakes assessing 71.19 nm in thickness and 5.48 µm in diameter, as well as a well-developed 0.4% vanadium-doped $Ni(OH)_2$ microflower with interconnected nanoflakes able to measure 71.19 nm in width and 5.48 µm in diameter. For the V-3 sample, increasing vanadium doping up to a specific value of '*d*' diminishes the crystallinity of the material, reducing the size of the microflower and increasing the thickness of nanoflakes. SEM analysis

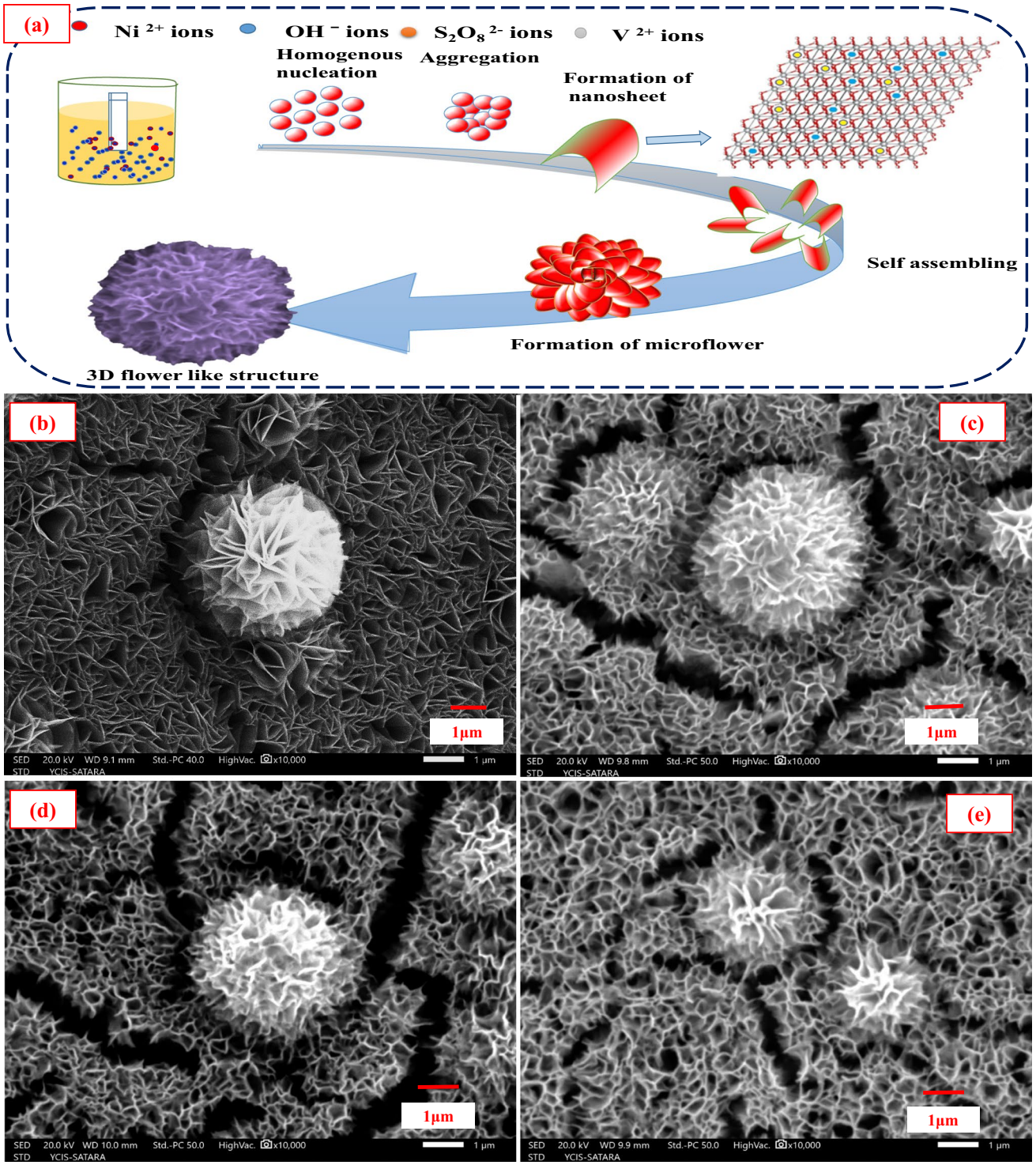

Fig. 4 **a** Schematic diagram of the formation of vanadium-doped $Ni(OH)_2$ nanoflakes then self-assembled microflower. Morphological study of vanadium-doped $Ni(OH)_2$ thin films for different doping concentrations (0.0%, 0.2%, 0.3%, and 0.4%) (**b**–**e**) respectively

reveals that the concentration of vanadium doping diameter of microflower increases. Sample V-2 has ultrathin nanoflakes and larger size microflower which provide a large surface area.

3.4 Electrochemical impedance spectroscopy

The Nyquist plot for the samples V-0, V-1, V-2, and V-3 electrodes is shown in Fig. 5a. The bode plot of all

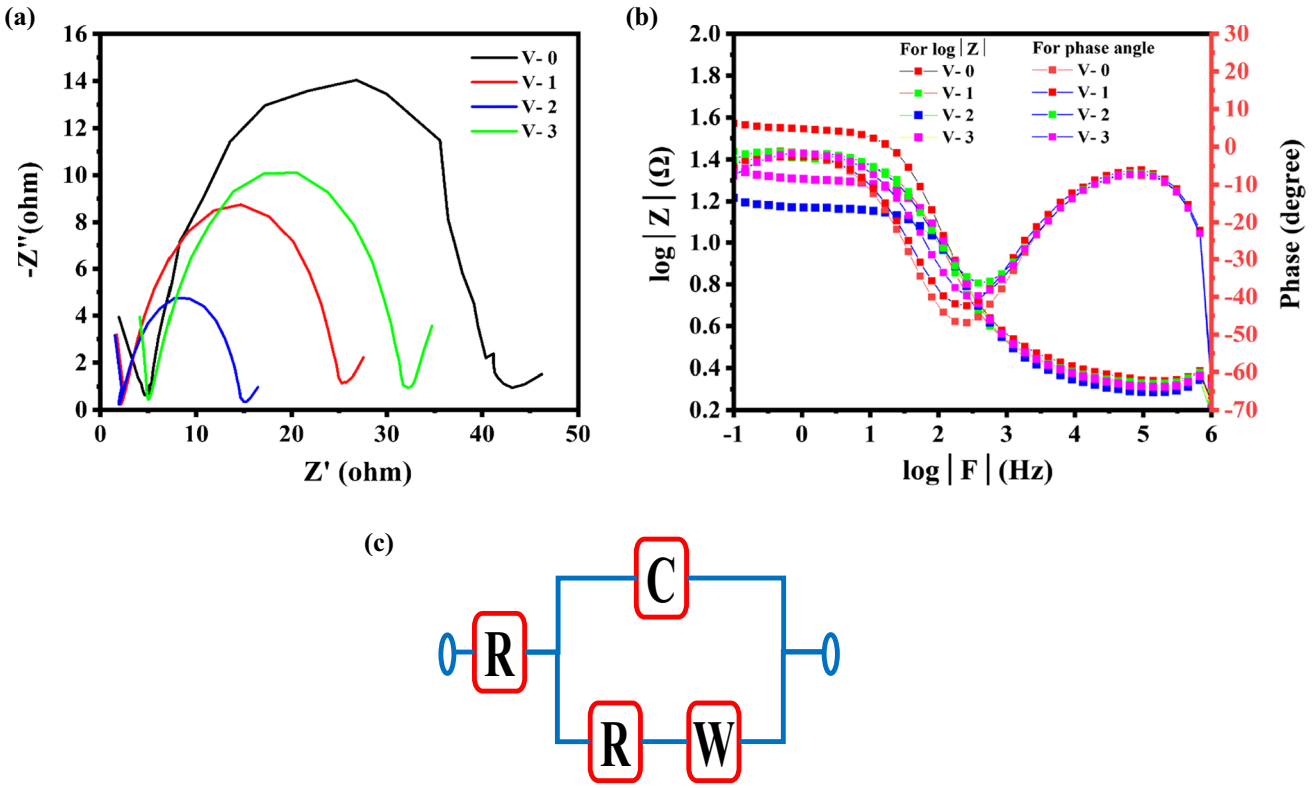

Fig. 5 Study of electrochemical impedance spectroscopy (EIS). **a** Nyquist plot of V-0, V-1, V-2, and V-3electrode. **b** Bode plot V-0, V-1, V-2, and V-3. **c** Equivalent circuit diagram

Table 1 EIS analysis for electrodes V-0, V-1, V-2, and V-3

Samples name/parameters	R_s (Ω cm^{-2})	C (F)	R_{ct} (Ω cm^{-2})	W
V-0	5.06	6.039×10^{-5}	38.11	0.2257
V-1	2.04	7.27×10^{-5}	23.52	0.228
V-2	2.56	7.21×10^{-5}	11.38	0.508
V-3	5.22	6.84×10^{-5}	26.78	0.1957

electrodes is shown in Fig. 5b. Equivalent circuits have two resistances one is solution resistance Rs and the other is charge transfer resistance Rct. The values of Rs and Rct for V-0, V-1, V-2, and V-3 are seen in Table 1. The solution resistance of each sample is approximately 3–5 Ω cm^{-2}. The charge transfer resistance of electrodes V-0, V-1, V-2, and V-3 are 38.11, 23.52, 11.38, and 26.78 Ω cm^{-2}, respectively. The charge transfer resistance of sample V-2 is the lowest value because of enhanced electric conductivity due to the optimum doping of vanadium into $Ni(OH)_2$ and its synergetic effect is seen in the electrochemical property [48]. The value of other components such as capacitance and, Warburg impedance is shown in Table 1.

3.5 Supercapacitor properties

Supercapacitor study of vanadium-doped $Ni(OH)_2$ electrode for various percentages of vanadium displayed in Fig. 6. Figure S1a–d shows the CV curves for the samples V-0, V-1, V-2, and V-3 at different scan rates 10, 20. 50. 80 and 100 mV s^{-1}. Figure 6a shows the CV curves of electrodes V-0, V-1, V-2, and V-3 at a scan rate of 1 mV s^{-1} and a potential window of 0.0 to 0.55 V vs SCE. For without a doping electrode, anodic peak and cathodic peaks observed at approximately 0.48 V and 0.25 V shifted after doping of vanadium. After observing the CV it can be seen that as the doping level increases, the vanadium ion is also contributing to an increase in the redox reaction in the area under the curve. The electrode with 0.3% vanadium doping has the maximum area under the curve. Because of the fast faradic reaction, cathodic and anodic peaks are observed on the cyclic voltammetry curve which postulates the battery type of material [49]. This redox reaction is given in Eq. 3.

$$\gamma - \mathrm{NiOOH} + \mathrm{H} + e^{+} \leftrightarrow \alpha - \mathrm{Ni(OH)_2} \quad (3)$$

During this process, γ-NiOOH accepts electron get reduced into α-$Ni(OH)_2$, and then α-$Ni(OH)_2$ donate its e^- gets oxidized

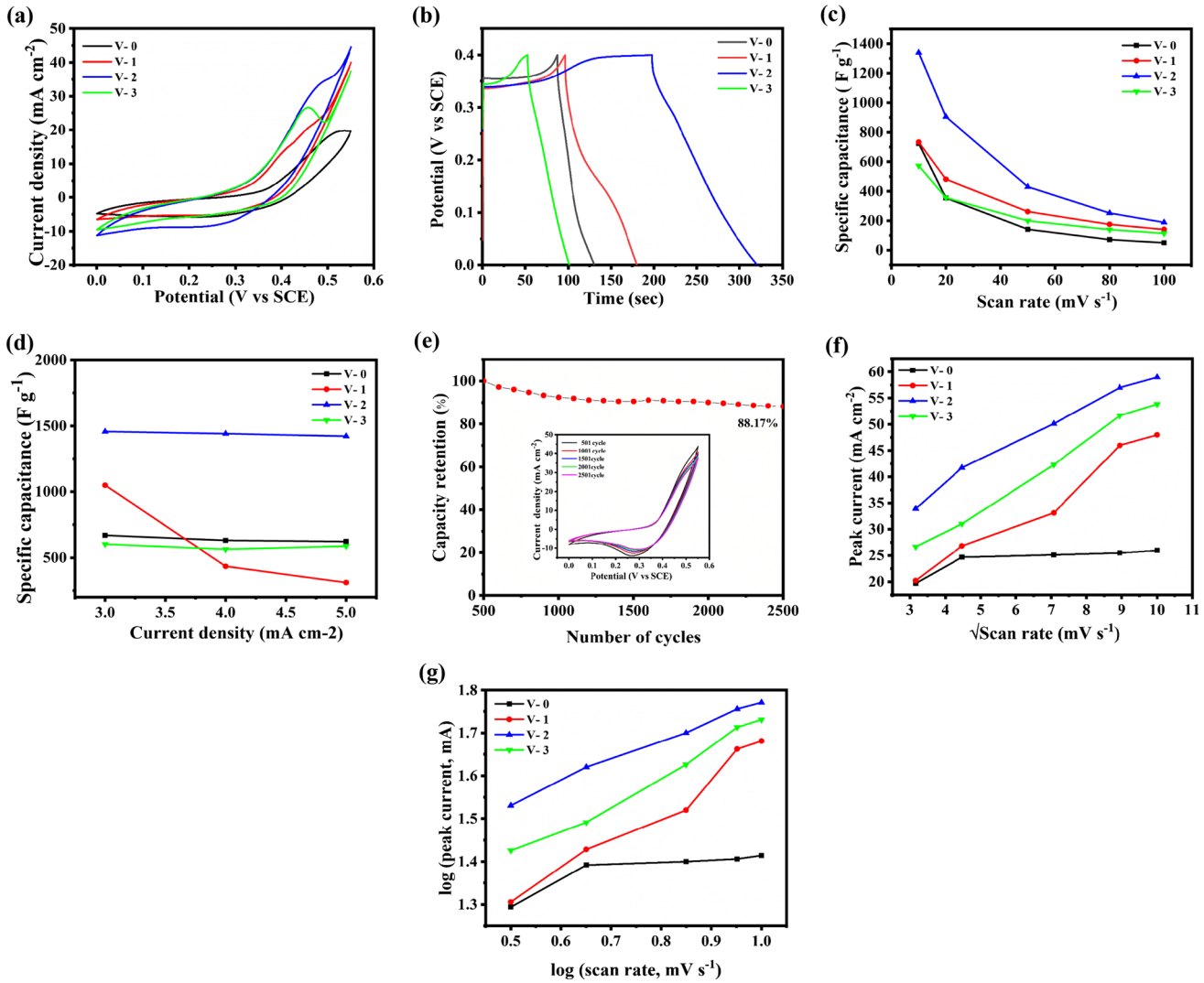

Fig. 6 Supercapacitor study of $Ni(OH)_2$ electrode for various deposition times. **a** The relative study CV curves of V-0, V-1, V-2, and V-3 electrodes with scanning rate 10 mVs^{-1}. **b** The relative study of GCD curves of $Ni(OH)_2$ thin film for various deposition times at current density 3 mA cm^{-2}. **c** Comparison of scan rate and specific capacitance of electrodes V-0, V-1, V-2, and V-3 electrodes. **d** Comparison of current density and specific capacitance of electrodes V-0, V-1, V-2, and V-3 electrodes. **e** The plot of capacity retention vs cycle number of V-2 sample. Inset: first five (black) and last five (red) charging-discharging cycles of 2000 cycles. **f** The plot of peak current vs square root of peak current. g The graph of the Log of peak current vs Log of scan rate

into γ-NiOOH [3, 50]. The maximum specific capacitance of electrodes V-0, V-1, V-2, and V-3 are 634, 733, 1339.8, and 573 F g^{-1} for a scan rate of 10 mV s^{-1}. Specific capacitance at various scan rates is represented in Fig. 6c. From these results, it can be inferred that the specific capacitance increases as the doping concentration increases but after a certain concentration the specific capacitance decreases [51, 52] 0.3% doping of vanadium has a better result as compared to other samples. The specific capacitance of 0.3% doping of vanadium is 1339.8, 905.2, 430, 252.7, and 189.44 F g^{-1} for scan rates 10, 20, 50, 80, and 100 mV s^{-1}. The GCD graph of electrodes V-0, V-1, V-2, and V-3 is shown in Fig S2a–d at different current densities of 3.0, 4.0, and 5.0 mA cm^{-2}. It reveals if the scan rate increases fast faradic redox reaction is carried out which cannot sustain by inner active sites which decreases specific capacitance [53, 54]. The difference in potential between anodic and cathodic peaks increases as the scan rate is enhanced. This describes the polarization and surface diffusion control processes at the electrode–electrolyte interface [23]. The GCD analysis for V-0, V-1, V-2, and V-3 samples is seen in Fig. 6 (b) at current densities of 3.0, mA cm^{-2}. The specific capacitances for the electrodes V-0, V-1, V-2, and V-3 at 3.0 mA cm^{-2} are 357.6, 741.3, 1456.87, and 603.12 F g^{-1}, respectively. The values of specific capacitance for the V-3 electrode are 1456.8, 1441, and 1421.8 F g^{-1} at current densities of 3.0, 4.0, and 5.0 mA cm^{-2}. A graph of

Table 2 A comparative study of present work and published work literature for supercapacitor application

Sr. No	Dopant	Specific Capacitance	Current density	Electrolyte	References
1	Cobalt	1421 F g^{-1}	6 A g^{-1}	1 M KOH	[22]
2	Cobalt	2879 F g^{-1}	1 A g^{-1}	1 M KOH	[56]
3	Yittrium	735 C g^{-1}	1.5 A g^{-1}	1 M KOH	[23]
4	Manganise	1498 C g^{-1}	2 A g^{-1}	6 M KOH	[26]
5	Aluminium	2122 F g^{-1}	1 A g^{-1}	6 M KOH	[57]
6	Cobalt	1366 F g^{-1}	1.5 A g^{-1}	6 M KOH	[58]
7	Carbon dots	155.57 mAh/g	40 A g^{-1}	1 M KOH	[59]
8	Vanadium	1456.8 F g^{-1}	3 mA cm^{-2}	1 M KOH	Present work

the change of specific capacitance for different current densities is displayed in Fig. 6d. Samples V-0, V-1, V-2, and V-3 have energy density 24.80, 23.32, 32.37 and 13.40 Wh kg^{-1}, respectively. Electrode V-2 has a maximum energy density of 32.37 Wh kg^{-1} at a power density of 1000 W kg^{-1}. Figure 6 (e) shows sample V-2 shows 88.5% retention after 1000 cycles at a scan rate of 100 mV s^{-1}. Figure 6f shows a graph square root of scan rate vs peak current. The slope of this plot gives the rate of diffusion. The slope of samples V-0, V-1, V-2, and V-3 is 4.14, 4.16, 5.95, and 3.79, respectively. So diffusion coefficients of all electrodes are 4.16 X 10^{-9}, 4.63×10^{-9}, 5.12×10^{-9}, and 4.54×10^{-9} cm s^{-1}. Electrode V-2 has a maximum diffusion coefficient which shows a larger rate of ion exchange. Figure 6g shows the graph log of scan rate vs the log of peak current. The slope of the graph shows the type of material. If the slope is less than 0.5, it shows battery type and if the slope is 1, it shows diffusion capacitive type behaviour [55]. So the slope of sample V-2 is approximately 0.5. Above analysis clear that the V-2 sample shows battery-type behavior. The structural, morphological, and structural study summarized as 0.3% doping of vanadium in $Ni(OH)_2$ shows better results. This sample has a maximum specific capacitance of 1456 F g^{-1} at a C.D of 3 mA cm^{-2} and 1338 F g^{-1} at a scan rate of 10 mV s^{-1}. The value of the diffusion coefficient of this sample is also maximum. From the EIS study Rs and Rct value of the sample, V-2 is small which greatly affects supercapacitor properties. The morphological properties also affect the electrochemical behavior of the material. Sample V-2 shows a larger size flower with ultrathin flakes which proved a larger area for electrode–electrolyte interaction. So, the V-2 sample shows enhance supercapacitor properties. Table 2 shows a comparisonal study between the present work and the issued literature work.

4 Conclusion

Vanadium-doped nickel hydroxide micro-flowers were successfully deposited by the chemical bath deposition method using nickel sulphate hexahydrate and vanadyl sulphate precursor. A hexagonal crystalline structure of $Ni(OH)_2$ was verified by XRD. But interlayer distance increases which approve the presence of vanadium in between layers. In the FT-IR study peak at 1023, 923 cm^{-1} approves the occurrence of the V=O bond. Morphology would not be majorly affected by variation of doping concentration but size, the number of flowers deposited and the thickness of nanoflakes change. The maximum specific capacitance of the V-2electrode is 1339.8 F g^{-1} from CV at 10 mV s^{-1} scan rates. The maximum specific capacitance of the V-2 electrode is 1456.8 F g^{-1} from GCD at the current density of 3.0 mA cm^{-2}. EIS study shows that electrode V-2 has the lowest charge transfer resistance (R_{ct}). The diffusion coefficient of electrode V-2 is 5.12×10^{-9} cm s^{-1} showing the maximum rate of ion exchange with electrolyte. Sample V-2 shows 88.5% retention after 1000 cycles at a scan rate of 100 mV s^{-1}. Based on the results, it is concluded that 0.3% vanadium doping enhances the electrochemical supercapacitor performance in terms of specific capacitance and stability.

Acknowledgements Dr. G. M. Lohar was thankful to DST-SERB for providing funds under the early career research award scheme fine no. ECR/2017/ 002099.

Data availability Data will be made available at reasonable request.

Declarations

Conflict of interest The author does not have any conflict of interest.

References

1. H. Sun, C. Wang, Z. Qi, W. Hu, Z. Zhang, Front. Chem. **8**, 1276 (2021)
2. Y. Zhu, C. Cao, S. Tao, W. Chu, Z. Wu, Y. Li, Sci. Rep. **4**, 1 (2014)
3. N.A. Alhebshi, R.B. Rakhi, H.N. Alshareef, J. Mater. Chem. A **1**, 14897 (2013)
4. S.B. Kulkarni, V.S. Jamadade, D.S. Dhawale, C.D. Lokhande, Appl. Surf. Sci. **255**, 8390 (2009)
5. G. Nagaraju, S.M. Cha, J.S. Yu, Sci. Rep. **7**, 1 (2017)
6. W. Wei, L. Mi, Y. Gao, Z. Zheng, W. Chen, X. Guan, Chem. Mater. **26**, 3418 (2014)

7. N.M. Santhosh, K.K. Upadhyay, P. Stražar, G. Filipič, J. Zavašnik, A. Mão De Ferro, R.P. Silva, E. Tatarova, M.F. de Montemor, U. Cvelbar, ACS Appl. Mater. Interfaces **13**, 20559 (2021)
8. F. Liu, X. Chu, H. Zhang, B. Zhang, H. Su, L. Jin, Z. Wang, H. Huang, W. Yang, Electrochim. Acta **269**, 102 (2018)
9. Z. Ge, Y.Q. Huo, D. Zheng, Q. Zhang, Int. J. Electrochem. Sci. **16**, 1 (2021)
10. Y. Wang, S. Gai, C. Li, F. He, M. Zhang, Y. Yan, P. Yang, Electrochim. Acta **90**, 673 (2013)
11. A. Gowrisankar, T. Selvaraju, Langmuir **37**, 5964 (2021)
12. O.C. Pore, A.V. Fulari, N.B. Velha, V.G. Parale, H.H. Park, R.V. Shejwal, V.J. Fulari, G.M. Lohar, Mater. Sci. Semicond. Process. **134**, 105980 (2021)
13. O.C. Pore, A.V. Fulari, S.H. Mujawar, R.V. Shejwal, V.J. Fulari, G.M. Lohar, Mater. Sci. Semicond. Process. **143**, 106550 (2022)
14. H. Hareendrakrishnakumar, R. Chulliyote, M.G. Joseph, J. Solid State Electrochem. **22**, 1 (2018)
15. M. Parashar, V.K. Shukla, R. Singh, J. Mater. Sci. Mater. Electron. **31**, 3729 (2020). (**315**)
16. M. Zhang, M. Drechsler, A.H.E. Müller, Chem. Mater. **16**, 537 (2004)
17. A. Muthuvel, M. Jothibas, C. Manoharan, Nanotechnol. Environ. Eng. **5**, 1 (2020). (**52**)
18. U.S. Mohanty, J. Appl. Electrochem. **2010**(41), 257 (2010). (**413**)
19. W. Zhang, X. Qiao, J. Chen, Mater. Sci. Eng. B **142**, 1 (2007)
20. A. Muthuvel, N.M. Said, M. Jothibas, K. Gurushankar, V. Mohana, J. Mater. Sci. Mater. Electron. **32**, 23522 (2021). (**3218**)
21. G. Kamarajan, D.B. Anburaj, V. Porkalai, A. Muthuvel, G. Nedunchezhian, J. Indian Chem. Soc. **99**, 100695 (2022)
22. D. Liang, S. Wu, J. Liu, Z. Tian, C. Liang, J. Mater. Chem. A **4**, 10609 (2016)
23. Y. Zhu, S. An, J. Cui, H. Qiu, X. Sun, Y. Zhang, W. He, CrystEngComm **21**, 4079 (2019)
24. R. Gu, X. Li, K. Cheng, L. Wen, RSC Adv. **9**, 25677 (2019)
25. K. Li, S. Li, F. Huang, Y. Lu, L. Wang, H. Chen, H. Zhang, Appl. Surf. Sci. **428**, 250 (2018)
26. Z. Zhang, H. Huo, L. Wang, S. Lou, L. Xiang, B. Xie, Q. Wang, C. Du, J. Wang, G. Yin, Chem. Eng. J. **412**, 128617 (2021)
27. N. Hussain, W. Yang, J. Dou, Y. Chen, Y. Qian, L. Xu, J. Mater. Chem. A **7**, 9656 (2019)
28. T.F. Zhang, W.J. Lee, S.H. Kwon, Z. Wan, Mater. Lett. **256**, 126656 (2019)
29. F. Azadian, A.C. Rastogi, Electrochim. Acta **330**, 135339 (2020)
30. G. Huang, C. Li, X. Sun, J. Bai, New J. Chem. **41**, 8977 (2017)
31. Z.H. Huang, Y. Song, X.X. Liu, Chem. Eng. J. **358**, 1529 (2019)
32. M. Sasidharan, N. Gunawardhana, M. Yoshio, K. Nakashima, J. Electrochem. Soc. **159**, A618 (2012)
33. S. Liang, Y. Hu, Z. Nie, H. Huang, T. Chen, A. Pan, G. Cao, Nano Energy **13**, 58 (2015)
34. H. Song, C. Zhang, Y. Liu, C. Liu, X. Nan, G. Cao, J. Power Sources **294**, 1 (2015)
35. X. Rui, Z. Lu, H. Yu, D. Yang, H.H. Hng, T.M. Lim, Q. Yan, Nanoscale **5**, 556 (2013)
36. L. Mai, L. Xu, C. Han, X. Xu, Y. Luo, S. Zhao, Y. Zhao, Nano Lett. **10**, 4750 (2010)
37. T. Zhai, H. Liu, H. Li, X. Fang, M. Liao, L. Li, H. Zhou, Y. Koide, Y. Bando, D. Golberg, Adv. Mater. **22**, 2547 (2010)
38. M. Lee, S.K. Balasingam, H.Y. Jeong, W.G. Hong, H.B.R. Lee, B.H. Kim, Y. Jun, Sci. Rep. **5**, 1 (2015)
39. M.T. Noori, M.M. Ghangrekar, C.K. Mukherjee, Int. J. Hydrogen Energy **41**, 3638 (2016)
40. Y. Zhang, Y. Zhao, W. An, L. Xing, Y. Gao, J. Liu, J. Mater. Chem. A **5**, 10039 (2017)
41. D.B. Mane, O.C. Pore, R.K. Kamble, D.V. Rupnavar, S.H. Mujawar, L.D. Kadam, R.V. Dhekale, G.M. Lohar, Appl. Phys. A **128**, 611 (2022)
42. R.E. Malekshah, B. Fahimirad, A. Khaleghian, Int. J. Nanomed. **15**, 2583 (2020)
43. A. Kalam, A.G. Al-Sehemi, A.S. Al-Shihri, G. Du, T. Ahmad, Mater. Charact. **68**, 77 (2012)
44. C. O'Dwyer, V. Lavayen, S.B. Newcomb, M.A. Santa Ana, E. Benavente, G. González, C.M. Sotomayor Torres, J. Electrochem. Soc. **154**, K29 (2007)
45. D. Navas, J.P. Donoso, C. Magon, C. M. Sotomayor-Torres, M. Moreno, H. Lozano, E. Benavente, G. González, New J. Chem. **43**, 17548 (2019)
46. Z. Sun, Z. Han, H. Liu, D. Wu, X. Wang, Renew. Energy **174**, 557 (2021)
47. D.B. Mane, O.C. Pore, R.K. Kamble, D.V. Rupnavar, S.H. Mujawar, L.D. Kadam, R.V. Dhekale, G.M. Lohar, Appl. Phys. A **128**, 1 (2022). (**1287**)
48. H.W. Park, B.K. Na, B.W. Cho, S.M. Park, K.C. Roh, Phys. Chem. Chem. Phys. **15**, 17626 (2013)
49. G.M. Lohar, R.K. Kamble, S.T. Punde, S.T. Jadhav, A.S. Patil, H.D. Dhaygude, B.P. Relekar, V.J. Fulari, Mater. Focus **5**, 481 (2016)
50. S.M. Pawar, A.I. Inamdar, K.V. Gurav, Y. Jo, H. Kim, J.H. Kim, H. Im, Mater. Lett. **141**, 336 (2015)
51. G.M. Lohar, O.C. Pore, A.V. Fulari, Ceram. Int. **47**, 16674 (2021)
52. Z. Zeng, P. Sun, J. Zhu, X. Zhu, Surf. Interfaces **8**, 73 (2017)
53. O.C. Pore, A.V. Fulari, V.G. Parale, H.H. Park, R.V. Shejwal, V.J. Fulari, G.M. Lohar, J. Porous Mater. **29**, 1991 (2022). (**296**)
54. R.B. Waghmode, A.P. Torane, J. Mater. Sci. Mater. Electron. **27**, 6133 (2016)
55. O.C. Pore, A.V. Fulari, R.V. Shejwal, V.J. Fulari, G.M. Lohar, Chem. Eng. J. **426**, 131544 (2021)
56. L. Liu, Y. Hou, Y. Gao, N. Yang, J. Liu, X. Wang, Electrochim. Acta **295**, 340 (2019)
57. J. Huang, T. Lei, X. Wei, X. Liu, T. Liu, D. Cao, J. Yin, G. Wang, J. Power Sources **232**, 370 (2013)
58. M.S. Vidhya, G. Ravi, R. Yuvakkumar, D. Velauthapillai, M. Thambidurai, C. Dang, B. Saravanakumar, RSC Adv. **10**, 19410 (2020)
59. C. Han, H. Si, S. Sang, K. Liu, H. Liu, Q. Wu, A.C.S. Appl, Nano Mater. **3**, 12106 (2020)